Millisecond-Timescale Monitoring of PbS Nanoparticle Nucleation and Growth Using Droplet-Based Microfluidics

*Ioannis Lignos, Stavros Stavrakis, Ardita Kilaj, and Andrew J. deMello**

The early-time kinetics (<1 s) of lead sulfide (PbS) quantum dot formation are probed using a novel droplet-based microfluidic platform, which allows for high-throughput and real-time optical analysis of the reactive process with millisecond time resolution. The reaction platform enables the concurrent investigation of the emission characteristics of PbS quantum dots and a real-time estimation of their size and concentration during nucleation and growth. These investigations reveal a two-stage mechanism for PbS nanoparticle formation. The first stage corresponds to the fast conversion of precursor species to PbS crystals, followed by the growth of the formed particles. The growth kinetics of the PbS nanoparticles follow the Lifshitz–Slyozov–Wagner model for Ostwald *ripening, allowing direct estimation of the rate constants for the process. In addition, the extraction of absorption spectra of ultrasmall quantum dots is demonstrated for first time in an online manner. The droplet-based microfluidic platform integrated with online spectroscopic analysis provides a new tool for the quantitative extraction of high temperature kinetics for systems with rapid nucleation and growth stages.*

1. Introduction

Nanocrystalline materials such as compound semiconductor nanoparticles have attracted significant interest owing to their tunable physicochemical properties and potential use as functional elements in photovoltaics,[1] energy storage,[1] medical imaging,[2,3] and biological sensing.[2,3] Unsurprisingly, over the last two decades there have been tremendous efforts to synthesize such colloidal crystals in an efficient, rapid, and controllable manner. Numerous studies have reported methods for the production of nanoparticles of defined size and shape.[4] However, the synthesis of "high quality" particle populations of well-defined size, shape and size distribution is a complex undertaking that typically requires the use of sophisticated experimental techniques together with a quantitative understanding of both nucleation and growth events.[5] Accordingly, a more complete understanding of the (synthetic) process of colloidal crystal formation would not only allow for the development of design rules for bespoke nanoparticle synthesis but also the avoidance of defects in the formed material.

The physical characteristics of semiconductor nanocrystals are in large part governed by quantum confinement effects with properties such as the optical band gap differing considerably from the bulk semiconductor.[1] Since these properties are ultimately regulated by the physical dimensions of the crystallite, there is considerable interest in developing robust synthetic strategies together with optical spectroscopies that allow an assessment of nucleation and growth kinetics.[5] Conventional macroscale reactors are typically used to synthesize nanoparticles using standard synthetic methods.[1] Indeed, flask-based methods have been used to synthesize a wide variety of quantum dots, such as CdSe,[6] CdS,[6] InP,[7,8] HgTe,[9] lead sulfide (PbS),[10–12] PbSe[12] and ternary/quaternary metal chalcogenide nanocrystals[13] using "hot injection" approaches. Unfortunately, the temporal and

I. Lignos, Dr. S. Stavrakis, A. Kilaj, Prof. A. J. deMello
Institute for Chemical and Bioengineering
Department of Chemistry and Applied Biosciences
ETH Zurich
Vladimir-Prelog-Weg 1, Zurich 8093, Switzerland
E-mail: andrew.demello@chem.ethz.ch

DOI: 10.1002/smll.201500119

spatial variation of physical conditions, such as temperature, pressure, and reagent concentration within macroscale reactors, has deleterious effects on both particle nucleation and growth.[5,14]

On a more general level, macroscale techniques are rather ineffective in providing information regarding nucleation and growth of nanocrystalline materials, since the extraction of kinetic data must typically be performed using offline analytical methods, such as transmission electron microscopy (TEM).[5] Many ex situ spectroscopic tools, such as absorption and fluorescence spectroscopy, X-ray scattering, and Fourier transform IR spectroscopy, have been used to characterize the growth mechanisms of semiconductor nanoparticles.[15,16] However, important information regarding the initial stages of the reaction (on the millisecond to second) timescale and its temporal evolution are normally inaccessible, since the reaction must be quenched prior to the analytical measurement. For this reason, quantitative assessments of reaction mechanisms are normally costly, complex and time-consuming endeavors, due to the need for large quantities of precursors and continuous washing of the formed particles.[5]

PbS quantum dots have a reduced band gap and exhibit exceptional electronic and optoelectronic properties for near-IR (NIR) applications.[17] Since their luminescence can span a broad spectrum of wavelengths in the NIR, they have found significant application in Schottky-based solar cells,[17–19] photodiodes[20] and in both in vitro and in vivo biological imaging.[21,22] It is surprising therefore that the mechanism of PbS nanoparticle formation, particularly at early reaction times, is relatively unexplored.[5] Since the synthesis of PbS nanoparticles with low size distributions can in principle be achieved by a detailed evaluation of the nucleation and growth stages, there is a recognized need for the integration of in situ optical detection techniques to allow the extraction of kinetic data. Importantly, there are literature reports describing real-time kinetic analysis of compound semiconductor nanoparticles in macroscale reactors.[23,24] Specifically, Qu et al. reported the in situ monitoring of the nucleation and growth of CdSe quantum dots using a fiber optic dip probe.[23] Size and concentration data could be extracted directly from absorption spectra, which were recorded with ms time resolution. Furthermore, the authors were able to probe the temporal evolution of photoluminescence (PL) emission, which in turn revealed that the reaction process involves particle size focusing and subsequent broadening of particle size distribution. However, issues with injection reproducibility, together with temperature variations within the reactor volume, led to uncertainties in the calculation of particle sizes and concentrations at very early timescales. Such issues highlight that the control of temperature, particle concentration and pressure are crucial in extracting precise kinetic data from such systems.

In recent years both continuous and segmented-flow microfluidic reactors have shown significant utility in synthetic chemistry.[14,25] Indeed, they have become popular tools in the production of quantum dots of exceptional quality.[14,26] The precise and rapid control of reaction temperatures, reaction times and reagent concentrations together with the integration of inline analytics are especially attractive for the quantitative analysis of nucleation and growth of colloidal nanoparticles.[25] The benefits of microfluidic technology have been extensively discussed in refs. [14,25], and [27] and allow the controllable formation of nanoparticle formulations of exceptional homogeneity, including CdS,[28,29] CdSe,[30–33] PbS,[19] PbSe,[19] SiO_2,[34,35] TiO_2,[36] Fe_3O_4,[37] Pd,[38] Ag,[39,40] and Au.[41,42] Amongst this growing list of applications are a small number of studies that report the integration of spectroscopic detection techniques[19,33,43–46] for reaction monitoring and optimization, as well as process automation.[33,47,48] Such methods include inline fluorescence spectroscopy[19,33,49] and X-ray scattering[50] using free space optics or integrated detectors. For example, Yue et al. demonstrated the integration of UV–vis absorption spectroscopy within a gas–liquid or liquid–liquid capillary reactor for real-time measurements of the size and concentration of gold nanoparticles.[43] The authors described two detection systems, either comprising a polyether ether ketone (PEEK) flow cell located downstream of the flow reactor or monolithically integrated waveguides. Using the latter they were able to extract average crystallite sizes and concentrations under variable flow conditions. Unfortunately, the use of such reactors does not allow for real-time absorption measurements at high temperatures (>100 °C) since detection is performed downstream of the heating zone. To this end, we recently demonstrated a microfluidic platform for the synthesis of monodisperse PbS and PbSe quantum dots in capillary reactors using inline NIR fluorescence spectroscopy.[19] The approach showed exceptional stability and reproducibility for the generation of nanoparticles emitting between 765 and 1580 nm and with fluorescence quantum efficiencies of up to 30%. However, such microfluidic platforms are best suited to probing reactions timescales larger than 1 s. Accordingly, the investigation of reaction kinetics at early times (<1 s) remains an unmet challenge. Herein, we report a novel approach for the online characterization of nucleation and growth (of PbS quantum dots) using a droplet-based microfluidic platform that integrates both visible and NIR (VIS/NIR) absorption and fluorescence spectroscopies (**Figure 1**). Significantly, online optical measurements can be performed during the heating phase, and thus high-throughput assays (with ms time resolution) can be achieved in a direct manner. To the best of our knowledge this represents the first use of droplet-based microfluidics for the real-time observation of the nucleation and growth at high temperatures.

2. Results and Discussion

2.1. Temperature Dependence of the Production Rate of PbS NCs

Figure 2A illustrates a series of online absorption spectra of synthesized PbS nanoparticles as a function of temperature with all the other reaction conditions kept constant (reaction time = 1 s, 1-octadecene (ODE)/oleic acid (OA) = 19, Pb/S = 1). As illustrated in Figure 2B, an increase in the operating temperature for a given reaction time results in a red-shift of the absorption maximum between 680 and 860 nm. Furthermore, Figure 2C demonstrates the evolution of the

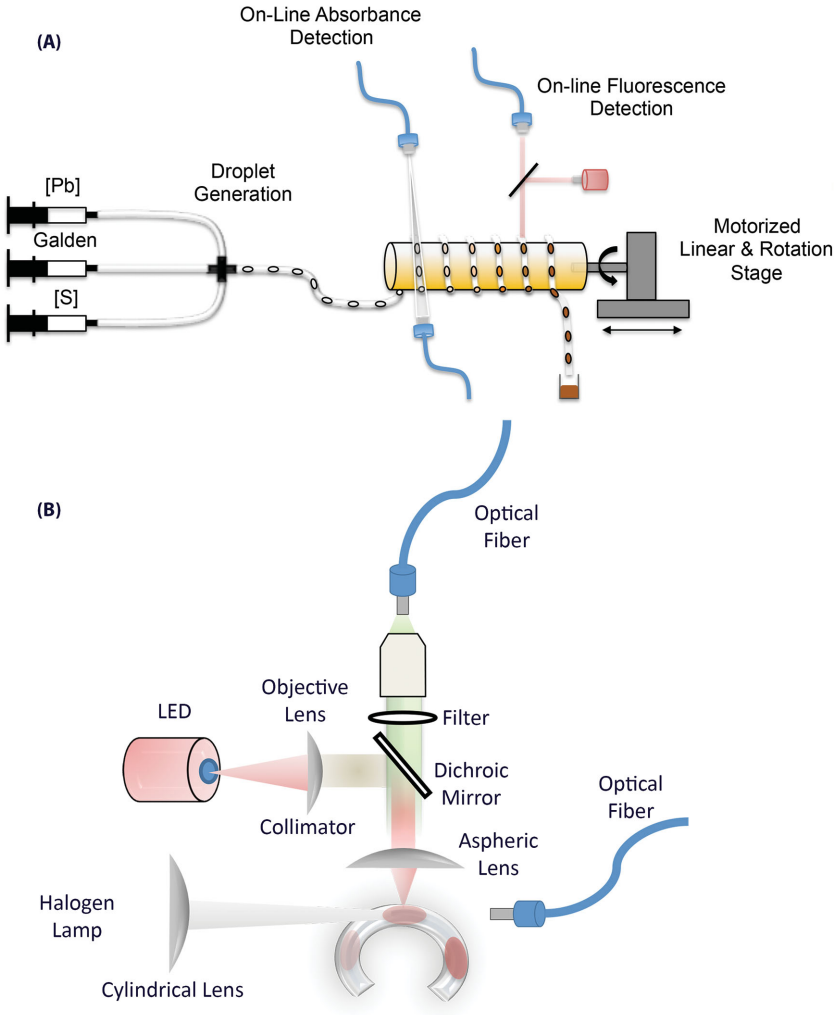

Figure 1. A) Schematic of the droplet-based microfluidic platform integrated with online absorbance and fluorescence detection for kinetic analysis of PbS quantum dot synthesis. B) Enlarged schematic view of the integrated optical system. This allows simultaneous performance of both absorbance and fluorescence analysis of droplets encapsulating the synthesized nanoparticles.

particle size, directly extracted from the peak absorbance using Equation(1), according to Cademartiri et al.[51]

$$E_g^*(\mathrm{eV}) = 0.41 + \frac{0.96}{(r(\mathrm{nm}))^2} + \frac{0.85}{(r(\mathrm{nm}))} \quad (1)$$

where r is the radius of the particle and E^*_g is the band gap. The concentration of the synthesized quantum dots was calculated using the Beer–Lambert law.[52] The extinction coefficient ε is size dependent and calculated according to Equation (2):

$$\varepsilon\left(M^{-1}\mathrm{cm}^{-1}\right) = 19600\left(r(\mathrm{nm})\right)^{2.32} \quad (2)$$

It is observed that increasing the temperature from 120 to 150 °C results in an increase in the mean PbS nanoparticle diameter from 2.35 to 2.9 nm. In addition, it is noticeable that high ODE/OA ratios (>11.5) together with low reaction times (<2 s) favor the synthesis of ultrasmall quantum dots (with diameters between 1.5 and 2.5 nm).

To assess the validity of inferring particle size in an online fashion, we used absorption measurements and Equations (1) and (2) to calculate the mean size of particles produced at a temperature of 90 °C (**Figure 3**A). This value was then compared to a TEM analysis of at least 1000 particles produced under the same conditions. The mean diameter of particles calculated from online absorption measurements was 3.9 nm, whilst the TEM analysis yielded a mean value of 4.1 ± 0.6 nm. This confirms the excellent correspondence between online absorbance measurements and offline TEM analysis.

2.2. Time-Resolved Measurements of Nucleation and Growth

Kinetic analysis of nanoparticle formation on millisecond timescales has previously been shown using stopped-flow methodologies.[53–55] Indeed, Brazeau et al. described a stopped-flow technique for the kinetic analysis of PbS nanoparticle synthesis.[56] In this study the authors utilized the aqueous reaction between $Pb(NO)_2$ and Na_2S at temperatures up to 45 °C. Successful interpretation of the kinetic mechanism was realized using both *Ostwald Ripening*[57,58] and *Oriented Attachment*[59] kinetic models. Unfortunately synthetic methods, for the formation of monodisperse PbS quantum dots, almost exclusively involve the adoption of high temperatures ranging from 80 to 160 °C and the use of toxic starting materials.[10,12,19,60] Stopped-flow systems most usually operate at low temperatures and require large assay volumes, whereas the described droplet-based microfluidic platform is well-suited for performing high-temperature colloidal syntheses consuming minimal volumes of reagent.[14] Additionally, the ability to generate and assay highly uniform droplets containing the same concentration of reagents via absorption and fluorescence spectroscopy, offers a direct route to the rapid extraction of kinetic information.

Figure 4 illustrates the evolution of extracted absorption spectra, together with the calculated size of the formed particles as a function of reaction time with all other experimental conditions (ODE/OA = 9, Pb/S = 1) being constant. Inspection of Figure 4A–E shows the redshift of the absorption maximum while increasing the reaction time for all tested operating temperatures. The average particle size at a given time and temperature was calculated according to Equation (1). Such an analysis confirmed that PbS quantum dots with a mean diameter between 2.7 and 3.5 nm could be reproducibly synthesized

www.MaterialsViews.com

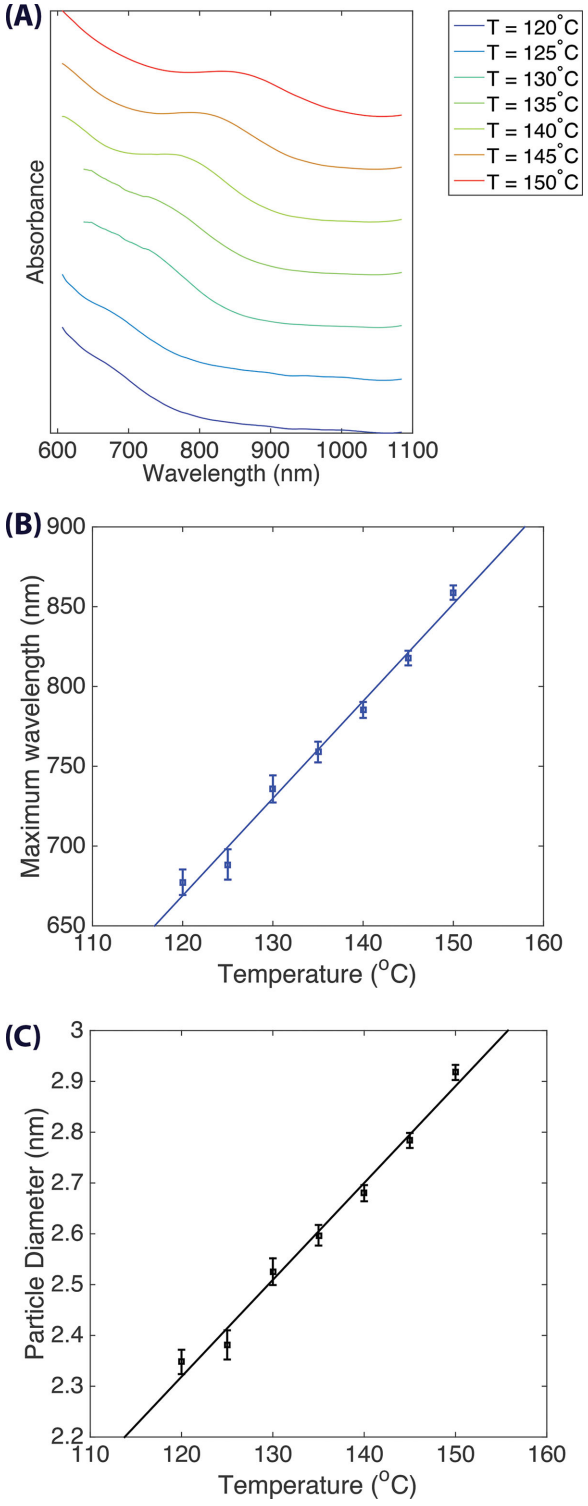

Figure 2. A) Online absorption spectra of PbS quantum dots at different operating temperatures (120–150 °C) after 1 s of reaction, variation of B) absorption maximum, and C) particle diameter as a function of temperature. All the other experimental parameters were fixed at $R{\cdot}t$ = 1 s, ODE/OA = 19, and Pb/S = 1.

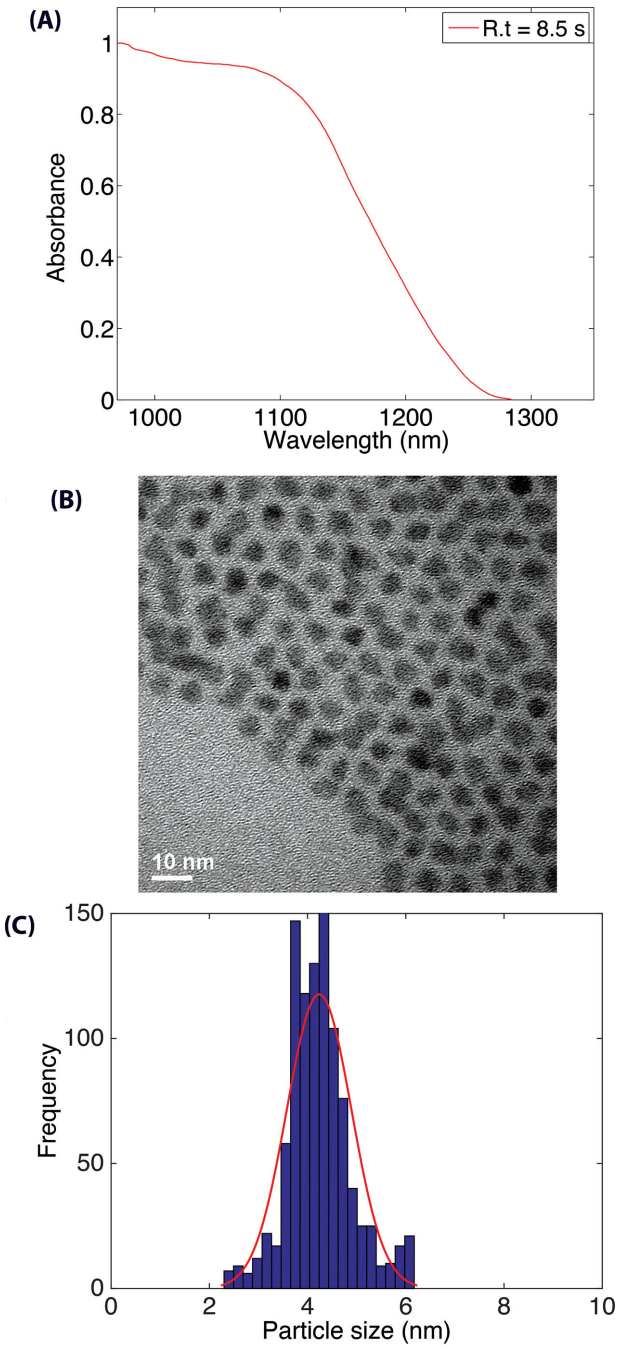

Figure 3. A) In situ NIR absorption spectrum of PbS quantum dots recorded after an 8.5 s reaction time (T = 90 °C, ODE/OA = 9, Pb/S = 1). The diameter of particles extrapolated from the online absorption measurement is calculated to be 3.9 nm. B) TEM image of a PbS nanoparticle population formed in the microfluidic platform under the same experimental conditions. The mean particle diameter is calculated to be 4.1 nm, with a standard deviation of 0.6 nm. C) Histogram of the nanoparticle size distribution. The histogram is produced by image analysis of TEM images.

within extremely short reaction times. At low operating temperatures (< 90 °C), the maxima of the first exciton peaks could be defined only after 3 s. It is noticeable from Figure 4I that the formation of particles having a mean diameter of 2.94 nm was observed only after 100 ms, with the particles growing to 3.35 nm over the next 1700 ms. Moreover, Figure 4F–K indicates that the growth rates increase rapidly as a function of temperature. Such behavior has been previously noted by Zhang et al. who investigated the dependence of the growth

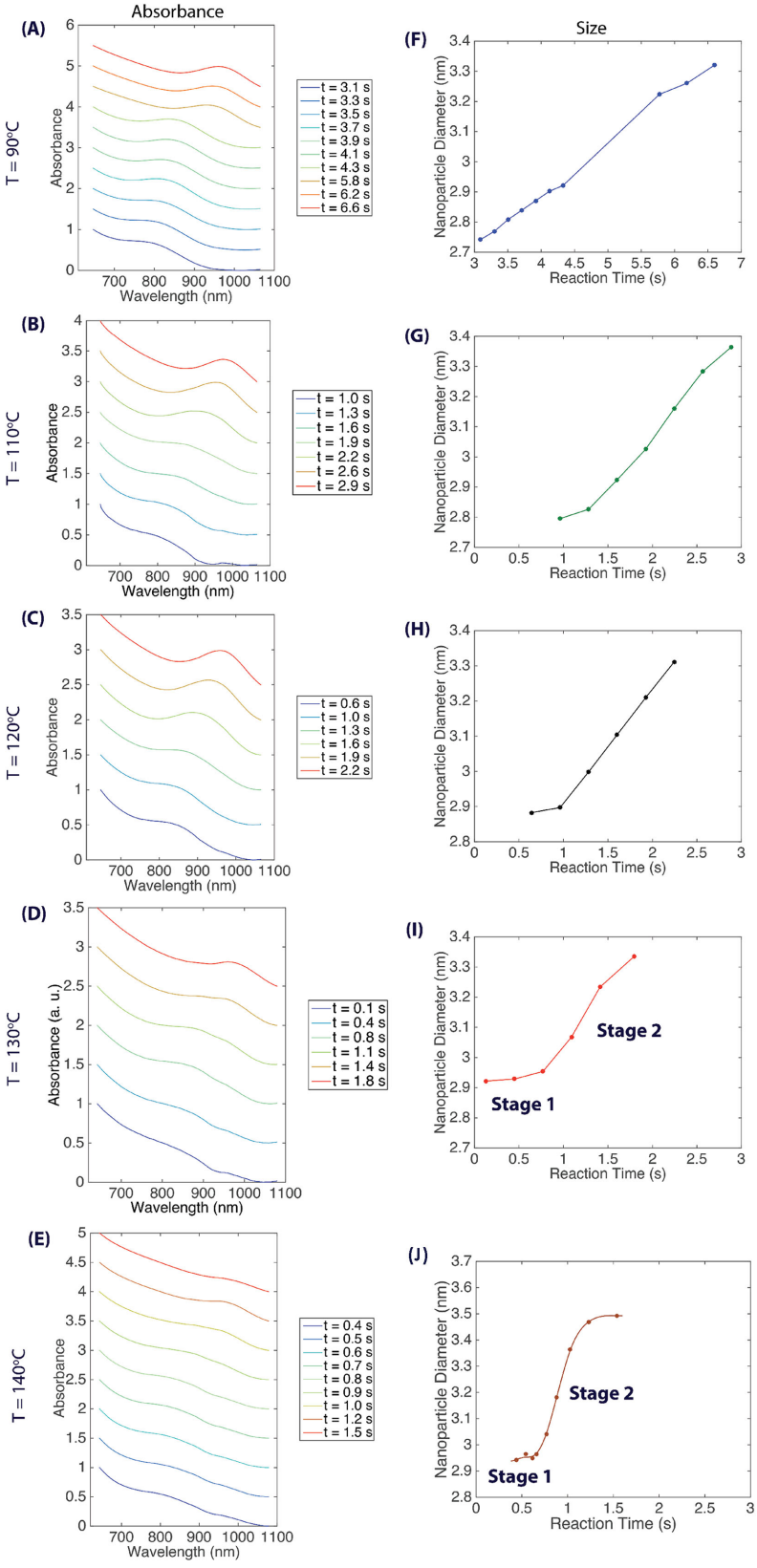

Figure 4. In situ observation of the nucleation and growth of PbS nanoparticles by real-time absorption measurements. A–E) Temporal evolution of the absorption spectra and F-J size of the synthesized PbS quantum dots by controlled tuning of the reaction time at four different temperatures (90, 110, 120, 130, and 140 °C) while all the other experimental parameters remained constant (ODE/OA = 9, Pb/S = 1). For the operating temperatures of 110, 120, and 130 °C, LSW equation was used only for the experimental points above 1 s, which indicates the growth regime. For 140 °C, the transition point was fixed at 0.7 s.

rate of quantum dots as a function of temperature.[12] In simple terms, the growth rate increases since higher temperatures favor the rapid consumption of monomers. However, it is also noticeable that the growth rate of the particles is markedly different at times below and above 0.7–1.2 s, depending on the operating temperature. As illustrated in Figure 4I, at times between 0 and 1 s (Stage 1), particle growth is much slower than for times above 1 s (Stage 2). To investigate such behavior, particle concentrations were calculated and shown in Figure S1 (Supporting Information). During Stage 1, the concentration of the formed nanoparticles increases dramatically to a maximum value of $\approx 2.9 \times 10^{-3}$ M L^{-1}. This suggests the continuous formation of new particles whose diameter remains constant at 2.94 nm in the first 1 s (nucleation stage). After a threshold concentration is reached, there is a subsequent decrease in the particle concentration with a concurrent linear increase in crystal size (growth stage). This behavior was clearly confirmed at higher operating temperatures (Figure 4K), while the transition point between stages was moved to 0.7 s. In addition, Figure S7 (Supporting Information) provides TEM images of the synthesized PbS nanoparticles after Stage 1 and Stage 2 while the operating temperature is set to 140 °C, which confirm our in situ calculations of the mean particle diameters. In Figure 4F–H, there were no defined absorption peaks below 0.8 s and accordingly extraction of particle diameter information was not feasible.

The linear behavior exhibited within Stage 2 can be understood using the *Lifshitz*, *Slyozov*, and *Wagner*[57,58] (LSW) model,

$$R(t)^3 - R(0)^3 = kt \tag{3}$$

Here R is the particle radius and k is the temperature dependent material constant. Ostwald Ripening is the dominant growth mechanism for PbS quantum dots, with ripening being controlled by volume diffusion in the liquid medium. Best fits for the temporal evolution of the cube of quantum dot radius for temperatures between 80 and 140 °C are shown in Figures S2 and S3 (Supporting Information). For each temperature, the rate constants of the synthesized quantum dots can be directly extracted by fitting to the LSW growth model (**Table 1**). It is noted that, growth in Stage 1 cannot be precisely described by existing kinetic models since there is a lack of experimental points at temperatures between 70 and 120 °C and reaction times below 500 ms.

Significantly, PL measurements were performed at the same time as absorption measurements for a variety of operating temperatures and reaction times. **Figure 5** shows the temporal evolution of the band edge emission spectrum of the formed nanoparticles together with its full-width-at-half-maximum (FWHM) at a temperature of 120 °C. It can be seen that the position of the PL maximum remains relatively constant until 1200 ms. For longer reaction times, the

Table 1. The values of k at different temperatures, which were extracted from the Ostwald Ripening model for the growth of PbS quantum dots.

T [°C]	k [nm s^{-1}]
80	0.37
90	0.59
110	1.07
120	1.17
130	1.27
140	1.49

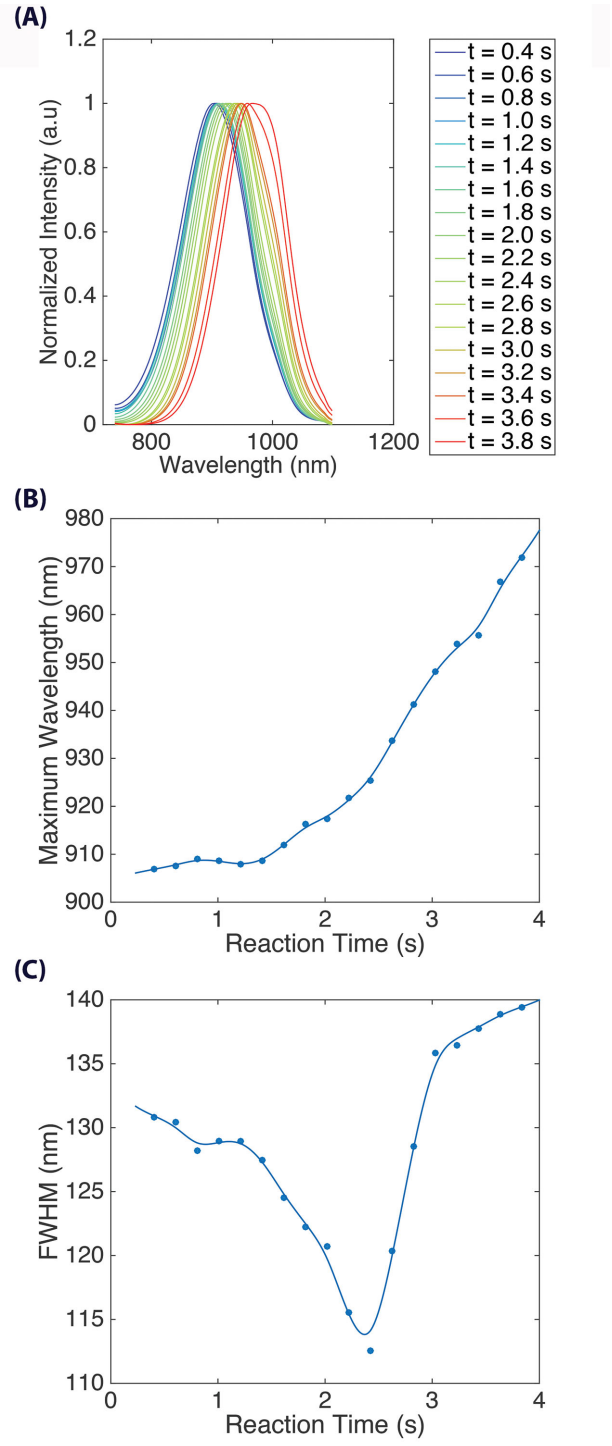

Figure 5. Temporal evolution of A) the photoluminescence emission spectra of the formed PbS nanoparticles, B) the peak wavelength of the band-edge emission, and C) the FWHM of the band-edge emission at a constant operating temperature of 120 °C, an ODE/OA ratio of 9 and a Pb/S ratio of 1.

band edge emission maximum shifts to longer wavelengths, indicating particle growth. Results from the real-time monitoring of absorption and PL spectra indicate a stepped kinetic mechanism composed of two stages as previously discussed. Additionally, Figure 5C demonstrates the evolution of the FWHM of the band edge emission over time. During Stage 1, the FWHM remains constant (128–130 nm), but decreases towards a minimum value of 112 nm during Stage 2, i.e., size focusing[19] of the formed nanoparticles. Above 2.6 s, the FWHM begins to increase, implying size broadening of the formed PbS quantum dots.

3. Conclusions

We have established a novel droplet-based microfluidic method for performing online kinetic measurements in high-temperature colloidal crystallization. Specifically, the microfluidic platform is successful in synthesizing PbS quantum dots of exceptional quality in an ultrafast manner, whilst also allowing quantitative kinetic measurements to be performed with ms resolution. Such developments have allowed the extraction of absorption spectra of ultrasmall quantum dots (with absorption maxima in the range of 650–750 nm) in an online fashion for the first time. Kinetic analysis indicates that at high operating temperatures the mechanism of PbS quantum dot formation is divided into two steps during early reaction times. In a first step (<1 s) nucleation occurs, where PbS particles of constant size are continuously formed. This is followed by a second stage involving growth of the formed particles with an overall concentration decrease. This second stage of the reaction is consistent with the Ostwald Ripening kinetic model providing the temperature-dependent material constants. This proposed mechanism was further confirmed by simultaneous PL measurements, which reveal both the focusing and broadening of the particle size distribution. Significantly, the microfluidic approach is applicable to the study of the fast kinetics of a wide range of nanomaterial syntheses and ion exchange reactions. Finally, we expect that combination of the proposed platform with novel chemistries will allow for fast and reliable extraction of the size, shape, and crystal structure of new colloidal nanoparticles.

4. Experimental Section

Microfluidic Reactor: Precision syringe pumps (neMESYS Low Pressure Syringe Pumps, Cetoni GmbH, Germany) were used to inject the dispersed (Pb and S precursor solutions) and the carrier fluids (Galden, Blaser Swisslube AG, Germany) into a PEEK cross (P-729, Upchurch Scientific, Germany) to form nanoliter droplets. The cross and the syringes carrying the precursor solutions where connected through polytetrafluoroethylene tubing (Internal Diameter (ID) 250 µm, Outer Diameter (OD) 1/16″, Upchurch Scientific, Germany) using PEEK fingertight fittings (F-127, Upchurch Scientific, Germany). The carrier fluid was transferred to the PEEK cross through fluorinated ethylene propylene tubing (ID 750 µm, OD 1/16″, Upchurch Scientific, Germany). The carrier and regent flow rates were kept fixed at 60 and 30 µL min^{-1}, respectively. The formed droplets containing the reaction mixture were subsequently directed through perfluoroalkoxy alkane (PFA) tubing (ID 500 µm, OD 1/16″, Upchurch Scientific, Germany) coiled around a copper-heating rod (diameter = 1.5 cm) to allow both the initiation of reaction and online detection of the formed PbS nanoparticles. The heating block was engraved using standard milling procedures to allow the tubing to sit within a defined groove (of radius 800 µm). The temperature of copper rod was controlled using a heating cartridge (6.5 × 40 mm, 100 W, Farnell, Switzerland), which was embedded inside the heating rod. The temperature was monitored using a thermocouple (Sensor, Thermolement Type K–0.5 mm, Farnell, Switzerland), which was inserted into the copper block close to the surface. Temperature control was realized using a proportional-integral-derivative (PID) controller (CN7800, Omega, USA) with an observed temperature variation from the set point of less than 0.1 °C. The heating rod was placed on top of a motorized rotation stage (CR1/M-Z7E, Thorlabs, Germany), which was also mounted on a motorized linear translation stage (MTS25/M-28E, Thorlabs, Germany). The axial and rotational movement of the heating rod was controlled using in house Labview software to ensure facile monitoring of the optical characteristics of the synthesized nanoparticles. By moving the heating rod at different positions, we can perform measurements at different points of the tubing. If you translate the tubing length to reaction time then the heating rod rotation provides access to very short reaction times (ms time frame) and the linear movement provides access to longer reaction times. It is important to note that the reactor design enables the simultaneous extraction of both optical absorption and fluorescence emission to quantitatively assay nucleation kinetics.

Online Photoluminescence Measurements: A red light-emitting diode (LED) (M625L3-Mounted High-Power LED, Thorlabs, Germany) was used as an excitation source for all fluorescence measurements (Figure 1B). The collimated beam was directed towards a dichroic beam splitter (Multiphoton LP-Strahlenteiler HC 665 LP, AHF, Germany) and then focused into the microfluidic channel using an aspheric lens (A240TM—f = 8.0 mm—Numerical aperture (NA) 0.50, Thorlabs, Germany). The emission originating from the microfluidic channel was collected by the same lens, passed through the dichroic beam splitter, a long-pass filter (635 LP Edge Basic Langpass-Filter, AHF, Germany) and coupled via a 10x objective (RMS10X—NA 0.25, Thorlabs, Germany) to a fiber spectrometer (PRo+, Ocean Optics, UK) through a 2 m long multimode fiber with a core diameter of 400 µm (QP100-2-UV-VIS, Ocean Optics, UK). The spectrometer comprised a 20 µm entrance slit, a 600 lines mm^{-1} grating and a detector containing 2048 pixels. The spectrometer was operated between 400 and 1100 nm, and data recorded using 100 ms integration time. The entire system was enclosed in a black box to minimize stray light pollution.

Online Absorbance Measurements: For all absorbance measurements a halogen lamp (HL-2000 HP, Ocean Optics, UK) was used as the illumination source. The output was collimated (F230SMA-C, Thorlabs, Germany) and shaped into a line oriented along the direction of flow via a planoconvex cylindrical lens (LJ4709RM, Thorlabs, Germany) having a focal length of 50 mm. Absorbance detection in droplet microfluidic reactors is challenging due to the limited optical pathlength determined by the inner capillary diameter. To circumvent sensitivity issues associated with reduced pathlengths, we implemented a geometry where a sheet of light propagates in a

tangential manner through the curved path of the tubing to approximately match the length of the reaction plugs (2 mm) (Figure 1B). Such an illumination profile maximizes the incident intensity, maintains illumination uniformity along the tubing and in turn minimizes contributions from stray light and scattering. A multimode fiber mounted on a three-axis stage platform and was placed along the optical axis of the light sheet to collect the transmitted light. The other end of the fiber was connected to either a visible or NIR spectrometer.

All collected data were analyzed using an in-house MATLAB algorithm. Each spectrum was generated from a weighted average of 300–600 scans with an integration time of 500–800 ms. To precisely define the absorption peak, the second derivative of the absorption spectrum was calculated (Figure S5, Supporting Information).

Materials: Lead(II) acetate trihydrate ($Pb(CH_3CO_2)_2{\cdot}3H_2O$, ≥99.99%, powder), bis(trimethylsilyl)sulfide (TMS_2S, synthetic grade), OA (90%), OA (99%) ODE (90%), ethanol over molecular sieve ($H_2O \leq 0.01\%$), and *n*-hexane absolute over molecular sieve ($H_2O \leq 0.01\%$) were purchased from Sigma-Aldrich, Switzerland and used as received. Toluene anhydrous (99.8%) was purchased from ABCR-Chemicals, Germany. Galden perfluoropolyether (PFPE) was purchased from Blaser Swisslube AG, Germany.

PbS Synthesis: In a three-neck flask, $PbAc_2{\cdot}3H_2O$ (1×10^{-3} M, 0.379 g), ODE (7.5–9.5 mL) and OA (2.5–0.5 mL) were dried at 120 °C under vacuum for 2 h to dissolve the lead salt and dry the solution. The solution was then allowed to cool before being loaded into a 10 mL gas-tight glass syringe (1000 Series, Hamilton). Under argon, the sulfur precursor solution was prepared by mixing TMS_2S (210 µL, 1×10^{-3} M) with ODE (20 mL). The solution was then loaded in a 10 mL gas-tight glass syringe (1000 Series, Hamilton). The Galden continuous phase was loaded in a 10 mL gas-tight glass syringe (1000 Series, Hamilton).

Offline QD Characterization: PbS particles were washed in air using anhydrous solvents. Hexane (300 µL) and ethanol (300 µL) were added to the crude solution followed by centrifugation to separate the quantum dots from the organic ligands. Obtained PbS quantum dots were redispersed in hexane, and again precipitated with ethanol for two additional washing steps and then redispersed in 300 µL of toluene. Samples were then dried under vacuum to remove toluene and redispersed in tetrachloroethylene for absorption and photoluminescence measurements. Transmission electron microscopy of the samples was carried out using a FEI Tecnai F30 microscope operating at 300 kV.

Supporting Information

Supporting Information is available from the Wiley Online Library or from the author.

Acknowledgements

The authors thank Olga Nazarenko for provision of the TEM micrographs. The work was partially supported by the Swiss National Science Foundation grant (200021_143638). The authors declare no competing financial interests.

[1] D. V. Talapin, J. S. Lee, M. V. Kovalenko, *Chem. Rev.* **2009**, *110*, 389.
[2] P. D. Howes, R. Chandrawati, M. M. Stevens, *Science* **2014**, *346*, 1247390.
[3] T. Sun, Y. S. Zhang, B. Pang, D. C. Hyun, M. Yang, Y. Xia, *Angew. Chem. Int. Ed.* **2014**, *53*, 12320.
[4] B. H. Kim, M. J. Hackett, J. Park, T. Hyeon, *Chem. Mater.* **2014**, *26*, 59.
[5] N. T. K. Thanh, N. Maclean, S. Mahiddine, *Chem. Rev.* **2014**, *114*, 7610.
[6] Z. A. Peng, X. Peng, *J. Am. Chem. Soc.* **2001**, *123*, 183.
[7] O. I. Micic, C. J. Curtis, K. M. Jones, J. R. Sprague, A. J. Nozik, *J. Phys. Chem.* **1994**, *98*, 4966.
[8] D. C. Gary, B. M. Cossairt, *Chem. Mater.* **2013**, *25*, 2463.
[9] M. V. Kovalenko, E. Kaufmann, D. Pachinger, J. Roither, M. Huber, J. Stangl, G. Hesser, F. Schäffler, W. Heiss, *J. Am. Chem. Soc.* **2006**, *128*, 3516.
[10] M. A. Hines, G. D. Scholes, *Adv. Mater.* **2003**, *15*, 1844.
[11] Y. Wang, A. Tang, K. Li, C. Yang, M. Wang, H. Ye, Y. Hou, F. Teng, *Langmuir* **2012**, *28*, 16436.
[12] J. Zhang, J. Gao, E. M. Miller, J. M. Luther, M. C. Beard, *ACS Nano* **2014**, *8*, 614.
[13] D. Aldakov, A. Lefrançois, P. Reiss, *J. Mater. Chem. C* **2013**, *1*, 3756.
[14] T. W. Phillips, I. G. Lignos, R. M. Maceiczyk, A. J. deMello, J. C. deMello, *Lab Chip* **2014**, *14*, 3172.
[15] X. Peng, J. Wickham, A. P. Alivisatos, *J. Am. Chem. Soc.* **1998**, *120*, 5343.
[16] J. S. Owen, E. M. Chan, H. Liu, A. P. Alivisatos, *J. Am. Chem. Soc.* **2010**, *132*, 18206.
[17] F. C. J. M van Veggel, *Chem. Mater.* **2014**, *26*, 111.
[18] C. Piliego, L. Protesescu, S. Z. Bisri, M. V. Kovalenko, M. A. Loi, *Energy Environ. Sci.* **2013**, *6*, 3054.
[19] I. Lignos, L. Protesescu, S. Stavrakis, L. Piveteau, M. J. Speirs, M. A. Loi, M. V. Kovalenko, A. J. deMello, *Chem. Mater.* **2014**, *26*, 2975.
[20] S. A. McDonald, G. Konstantatos, S. Zhang, P. W. Cyr, E. J. D. Klem, L. Levina, E. H. Sargent, *Nat. Mater.* **2005**, *4*, 138.
[21] M. Corricelli, N. Depalo, E. Di Carlo, E. Fanizza, V. Laquintana, N. Denora, A. Agostiano, M. Striccoli, M. L. Curri, *Nanoscale* **2014**, *6*, 7924.
[22] K. Wu, J. Zhang, S. Fan, J. Li, C. Zhang, K. Qiao, L. Qian, J. Han, J. Tang, S. Wang, *Chem. Commun.* **2014**, *51*, 141.
[23] L. Qu, W. W. Yu, X. Peng, *Nano Lett.* **2004**, *4*, 465.
[24] K. Yu, J. Ouyang, D. M. Leek, *Small* **2011**, *7*, 2250.
[25] K. S. Elvira, X. Casadevall i Solvas, R. C. R. Wootton, A. J. deMello, *Nat. Chem.* **2013**, *5*, 905.
[26] A. M. Nightingale, J. C. de Mello, *J. Mater. Chem.* **2010**, *20*, 8454.
[27] K. F. Jensen, B. J. Reizman, S. G. Newman, *Lab Chip* **2014**, *14*, 3206.
[28] J. B. Edel, R. Fortt, J. C. deMello, A. J. deMello, Chem. Commun. **2002**, 1136.
[29] A. L. Abdelhady, M. Afzaal, M. A. Malik, P. O'Brien, *J. Mater. Chem.* **2011**, *21*, 18768.
[30] E. M. Chan, A. P. Alivisatos, R. A. Mathies, *J. Am. Chem. Soc.* **2005**, *127*, 13854.
[31] S. Krishnadasan, J. Tovilla, R. Vilar, A. J. deMello, J. C. deMello, *J. Mater. Chem.* **2004**, *14*, 2655.
[32] A. M. Nightingale, T. W. Phillips, J. H. Bannock, J. C. de Mello, *Nat. Commun.* **2014**, *5*, 377.

[33] R. M. Maceiczyk, A. J. deMello, *J. Phys. Chem. C* **2014**, *118*, 20026.
[34] S. A. Khan, A. Günther, M. A. Schmidt, K. F. Jensen, *Langmuir* **2004**, *20*, 8604.
[35] J. B. Wacker, I. Lignos, V. K. Parashar, M. A. M. Gijs, *Lab Chip* **2012**, *12*, 3111.
[36] E. Y. Erdem, J. C. Cheng, F. M. Doyle, A. P. Pisano, *Small* **2013**, *10*, 1076.
[37] K. Kumar, A. M. Nightingale, S. H. Krishnadasan, N. Kamaly, M. Wylenzinska-Arridge, K. Zeissler, W. R. Branford, E. Ware, A. J. deMello, J. C. deMello, *J. Mater. Chem.* **2012**, *22*, 4704.
[38] Y. H. Kim, L. Zhang, T. Yu, M. Jin, D. Qin, Y. Xia, *Small* **2013**, *9*, 3462.
[39] L. Zhang, Y. Wang, L. Tong, Y. Xia, *Langmuir* **2013**, *29*, 15719.
[40] J. E. Q. Quinsaat, A. Testino, S. Pin, T. Huthwelker, F. A. Nüesch, P. Bowen, H. Hofmann, C. Ludwig, D. M. Opris, *J. Phys. Chem. C* **2014**, *118*, 11093.
[41] V. Sebastian Cabeza, S. Kuhn, A. A. Kulkarni, K. F. Jensen, *Langmuir* **2012**, *28*, 7007.
[42] S. A. Khan, S. Duraiswamy, *Lab Chip* **2012**, *12*, 1807.
[43] J. Yue, F. H. Falke, J. C. Schouten, T. A. Nijhuis, *Lab Chip* **2013**, *13*, 4855.
[44] S. Krishnadasan, J. Tovilla, R. Vilar, A. J. deMello, J. C. deMello, *J. Mater. Chem.* **2004**, *14*, 2655.
[45] A. M. Nightingale, S. H. Krishnadasan, D. Berhanu, X. Niu, C. Drury, R. McIntyre, E. Valsami-Jones, J. C. deMello, *Lab Chip* **2011**, *11*, 1221.
[46] S. Yao, Y. Shu, Y.-J. Yang, X. Yu, D.-W. Pang, Z.-L. Zhang, *Chem. Commun.* **2013**, *49*, 7114.
[47] S. Krishnadasan, R. J. C. Brown, A. J. deMello, J. C. deMello, *Lab Chip* **2007**, *7*, 1434.
[48] A. Toyota, H. Nakamura, H. Ozono, K. Yamashita, M. Uehara, H. Maeda, *J. Phys. Chem. C* **2010**, *114*, 7527.
[49] E. M. Chan, R. A. Mathies, A. P. Alivisatos, *Nano Lett.* **2003**, *3*, 199.
[50] J. Polte, R. Erler, A. F. Thünemann, S. Sokolov, T. T. Ahner, K. Rademann, F. Emmerling, R. Kraehnert, *ACS Nano* **2010**, *4*, 1076.
[51] L. Cademartiri, E. Montanari, G. Calestani, A. Migliori, A. Guagliardi, G. A. Ozin, *J. Am. Chem. Soc.* **2006**, *128*, 10337.
[52] W. W. Yu, L. Qu, W. Guo, X. Peng, *Chem. Mater.* **2004**, *16*, 560.
[53] F. Huang, H. Zhang, J. F. Banfield, *J. Phys. Chem. B* **2003**, *107*, 10470.
[54] F. Huang, H. Zhang, J. F. Banfield, *Nano Lett.* **2003**, *3*, 373.
[55] M. Tiemann, F. Marlow, J. Hartikainen, Ö. Weiß, M. Linden, *J. Phys. Chem. C* **2008**, *112*, 1463.
[56] A. L. Brazeau, N. D. Jones, *J. Phys. Chem. C* **2009**, *113*, 20246.
[57] I. M. Lifshitz, V. V. Slyozov, *J. Phys. Chem. Solids* **1961**, *19*, 35.
[58] C. Wagner, *Z. Electrochem.* **1961**, *65*, 581.
[59] R. L. Penn, J. F. Banfield, *Science* **1998**, *281*, 969.
[60] I. Moreels, K. Lambert, D. Smeets, D. De Muynck, T. Nollet, J. C. Martins, F. Vanhaecke, A. Vantomme, C. Delerue, G. Allan, Z. Hens, *ACS Nano* **2009**, *3*, 3023.

Received: January 15, 2015
Revised: April 1, 2015
Published online: May 21, 2015